Acta Oceanol. Sin., 2020, Vol. 39, No. 11, P. 82–90
https://doi.org/10.1007/s13131-020-1669-y
http://www.hyxb.org.cn
E-mail: hyxbe@263.net

Variations of mesoscale eddy SST fronts based on an automatic detection method in the northern South China Sea

Chunhua Qiu[1, 2*], Juan Ouyang[1], Jiancheng Yu[3], Huabin Mao[4], Yongfeng Qi[4], Jiaxue Wu[1, 2*], Danyi Su[1]

[1] School of Marine Sciences, Sun Yat-sen University, Guangzhou 510275, China

[2] Southern Marine Science and Engineering Guangdong Laboratory (Zhuhai), Zhuhai 519020, China

[3] State Key Laboratory of Robotics, Shenyang Institute of Automation, Chinese Academy of Sciences, Shenyang 110016, China

[4] State Key Laboratory of Tropical Oceanography, South China Sea Institute of Oceanology, Chinese Academy of Sciences, Guangzhou 510301, China

Received 15 June 2020; accepted 22 July 2020

Abstract

SST fronts at the mesoscale eddy edge (ME fronts) were investigated from 2007–2017 in the northern South China Sea (NSCS) based on an automatic method using satellite sea level anomaly (SLA) and SST data. The relative probabilities between the number of anticyclonic/cyclonic ME fronts (AEF/CEF) and the number of anticyclones/cyclones reached 20%. The northeastern and southwestern parts of these anticyclones had more fronts than the northwestern and southeastern parts, although CEFs were nearly equally distributed in all directions. The number of ME fronts had remarkable seasonal variations, while the eddy kinetic energy (EKE) showed no seasonal variations. The total EKE at the ME fronts was three times of that within the MEs, and it was much stronger in AEFs than in CEFs. The interannual variability in the number of ME fronts and EKE had no significant correlation with the El Niño-Southern Oscillation (ENSO) index. Possible mechanisms of ME fronts were discussed, but the contributions of mesoscale eddies to SST fronts need to be quantified in future studies.

Key words: detection method, mesoscale eddy SST front, northern South China Sea

Citation: Qiu Chunhua, Ouyang Juan, Yu Jiancheng, Mao Huabin, Qi Yongfeng, Wu Jiaxue, Su Danyi. 2020. Variations of mesoscale eddy SST fronts based on an automatic detection method in the northern South China Sea. Acta Oceanologica Sinica, 39(11): 82–90, doi: 10.1007/s13131-020-1669-y

1 Introduction

Oceanic fronts, or transition zones between water masses, play important roles in regulating oceanic heat, energy, and matter balances through associated vertical transport (Lévy et al., 2001; Ruiz et al., 2019). They also influence the atmospheric boundary layer (Xie, 2004). The observation and modeling of oceanic fronts are topics of interest in oceanography.

The South China Sea (SCS) is a large marginal sea in the tropical western Pacific Ocean. The complex topography and monsoon allow multiscale oceanic structures to prevail in the SCS; these include branches of the Kuroshio Current and the SCS Warm Current as well as western boundary currents, mesoscale eddies (MEs), river plumes, upwelling, and submesoscale structures (Hu et al., 2012; Yuan et al., 2006; Zhong et al., 2017; Feng et al., 2020). Fronts have been detected in the above structures, i.e., Kuroshio fronts (Liu et al., 2017), upwelling fronts (Jing et al., 2015), and river plume fronts (Qiu et al., 2017a). Seasonal variations of above thermal fronts were first statistically revealed by Wang et al. (2001), who found that thermal fronts were strong in winter to spring and weak in summer to autumn. In addition to the above fronts, which have lifetimes longer than one month, there are other fronts with temporal scales less than 30 d in the SCS (Hosoda et al., 2012), which might be induced by MEs, filaments and so on.

MEs are common in the SCS. The horizontal lengths/time scales of MEs are 50–300 km/1–10 months (Capet et al., 2008; McWilliams, 2016). Their horizontal scales of motion are characterized by baroclinic instability, at which the Rossby number $Ro=\frac{V}{fL}<1$, where V and L are horizontal velocity and length scales, respectively, and f is the Coriolis frequency (Torres et al., 2018). Qiu et al. (2017a) found that the length scales depended on the local energy of MEs. One high eddy kinetic energy (EKE) band occurred in the northern SCS (NSCS), where both the number of MEs and the EKEs have no significant seasonal variations (Chen et al., 2009; Cheng and Qi, 2010). Interannual variations in EKE were suggested to be induced by the El Niño-Southern Oscillation (ENSO), which show a negative correlation between the SCS EKE and the ENSO index through conveying Kuroshio transport (Sun et al., 2016) or wind stress curl (Wang et al., 2008; Cheng and Qi, 2010). MEs deform with asymmetric shapes during propagation (Wang et al., 2018; Qiu et al., 2019b), resulting in strong vertical currents and turbulence at the ME boundary associated with thermal fronts (Yang et al., 2017, 2019; Qiu et al., 2019a).

The signals of strong coastal and Kuroshio fronts in winter and strong upwelling and river plume fronts in summer hide the high-frequency frontal signals in seasonal variation studies (Wang et al., 2001; Jing et al., 2015; Qiu et al., 2017a). The SST

Foundation item: The National Natural Science Foundation of China under contract No. 41976002.
*Corresponding author, E-mail: qiuchh3@mail.sysu.edu.cn; wujiaxue@mail.sysu.edu.cn

fronts at the mesoscale eddy edge (hereafter, ME fronts) are expected to have high-frequency variations, because MEs easily deform and propagate at a mean speed of ~0.1 m/s (Chen et al., 2009; Su et al., 2020). As anticyclones have negative vorticity and cyclones have positive vorticity, the numbers of generated anticyclones and cyclones exhibit different seasonal variations due to monsoon-driven wind stress curl (Chen et al., 2009; Wang et al., 2008), which may influence the ME front. In this study, we examine the characteristics and possible mechanisms of ME fronts to better understand the interaction between MEs and SST fronts and improve our understanding of oceanic physical processes in the NSCS.

The data and methods are presented in Section 2, ME fronts identified from the observation data are presented in Section 3, statistical analyses are presented in Section 4, possible mechanisms for ME fronts are presented in Section 5, and summaries are presented in Section 6.

2 Data and methods

2.1 *Data*

2.1.1 *Chinese underwater glider data*

To investigate the structures at ME fronts, we collected observations from an underwater glider. The Chinese underwater glider was designed by the Shenyang Institute of Automation, Chinese Academy of Sciences, and named "Sea wing". "Sea wing" underwater gliders have been successfully used to investigate sea surface cooling (Qiu et al., 2015), mesoscale eddies (Shu et al., 2016; Qiu et al., 2019b), and submesoscale eddies (Qiu et al., 2019a). The underwater glider captured 205 vertical profiles of temperature, salinity and pressure from April 19 to June 15, 2015. We interpolated the temperature and salinity to a 1-m vertical resolution.

2.1.2 *Reanalysis data*

We used the HYbrid Coordinate Ocean Model (HYCOM), a data-assimilative hybrid isopycnal-sigma-pressure (generalized) coordinate ocean model, to calculate vertical velocity within the MEs. Descriptions of the data set are presented at https://www.hycom.org/. The data comprise 33 vertical levels at (1/12)° horizontal resolution. HYCOM data have been successfully used to observe MEs in the NSCS (Zhang et al., 2013; Huang et al., 2017).

2.1.3 *Satellite data*

We used the operational SST and sea ice analysis (OSTIA) SST products to detect SST fronts. OSTIA SST products are a combination of microwaves, infrared satellite measurements, and *in situ* SST data available over global telecommunications system products (Donlon et al., 2011). Products from 2007 to 2017 with daily temporal resolution and ~5 km spatial resolution were downloaded from ftp://ftp.nodc.noaa.gov/pub/data.nodc/ghrsst/L4/GLOB/UKMO/OSTIA/.

Sea level anomaly (SLA) data are merged products of ERS-1/2, TOPEX/Poseidon, Jason-1/2, and envisat altimeters from the archiving, validation and interpretation of satellite oceanographic data (AVISO) dataset. SLAs represent variations in the sea surface heights relative to the mean sea surface based on a 20-year (1993–2012) reference period. The product has daily records and 0.25°×0.25° resolution. To match the date range of OSTIA SSTs, we used SLA data from 2007 to 2017.

2.2 *Identification method of the ME front*

To identify the ME front, we first identified the ME and SST fronts separately, and then matched the ME and the associated SST front. The data used here are AVISO SLA and OSTIA SST from 2007 to 2017. The flowchart is shown in Fig. 1.

2.2.1 *Identification of mesoscale eddies*

To identify the MEs, we used a winding-angle (WA) algorithm, which detects eddies with greater efficiency, recognition accuracy, and stability (Sadarjoen and Post, 2000; Chaigneau et al., 2008). The WA algorithm searches for local maximum (minimum) SLA values that correspond to potential centers of anticyclonic (cyclonic) eddies in every 4°×4° grid window. Closed streamlines that belong to the same eddy are then selected and clustered by calculating the streamline WA. This algorithm is described in greater detail in Sadarjoen and Post (2000). We used this automatic method to identify MEs in 2007–2017 and obtained 93 anticyclones and 67 cyclones. Then we produced a data array of ME parameters, including ME center, radius, EKE, and shear stress. The identified mesoscale eddy on May 30, 2015 is shown in Fig. 1c.

2.2.2 *SST Front detection*

We used the maximum gradient magnitude method to detect the SST fronts. Previous studies have used this method to detect SST fronts in the NSCS (Wang et al., 2001; Qiu et al., 2017a). First, we calculated the SST gradient magnitude for pixels (x, y, t) in eight directions from 0° to 360° at 45° intervals, and then we obtained the maximum SST gradient magnitude among the eight directions as $\mathrm{GM}_{\max}(x, y, t)$. One case of SST gradient magnitude map is shown in Fig. 1d. Pixels for which $\mathrm{GM}_{\max}(x, y, t) \geqslant 0.2$°C/km were identified as frontal pixels and defined as $f(x, y, t)$=1; others were defined as $f(x, y, t)$=0.

2.2.3 *Identification of the ME fronts*

To determine the ME front position, we defined a search radius, r, for each mesoscale eddy. Then, we assumed that the eddy center located at position (x_0, y_0) at time t and the radius of the mesoscale eddy is r_0. Thus, the distance between an arbitrary position $r(x, y, t)$ and eddy center (x_0, y_0) is,

$$r^2(x, y, t) = (x - x_0)^2 + (y - y_0)^2, \quad t = 1, 2, 3, \cdots, N. \tag{1}$$

$\mathrm{ME}(x, y, t)$ is defined as the mesoscale eddy index. Within the search radius of $\frac{3}{2} r_0(x_0, y_0, t)$, we assumed all the pixels are ME pixels, and denoted them as $\mathrm{ME}(x, y, t) = 1$. Beyond this range, $\mathrm{ME}(x, y, t) = 0$. That is the pixel (x, y, t) with $\mathrm{ME}(x, y, t) = 1$ is an ME pixel.

Then, we matched the MEs and SST fronts. Under the conditions of $\frac{3r_0(x_0, y_0, t)}{2} > r(x, y, t) > \frac{r_0(x_0, y_0, t)}{2}$, $\mathrm{ME}(x, y, t) = 1$, and $f(x, y, t) = 1$, pixel (x, y, t) is taken as an ME frontal pixel and marked as $\mathrm{MEF}(x, y, t) = 1$; otherwise, $\mathrm{MEF}(x, y, t) = 0$.

Finally, the absolute probability of the ME front, $P(x, y)$, is defined as the count of ME front divided by the sample numbers,

$$P(x, y) = \frac{\sum_{t=1}^{N} \mathrm{MEF}(x, y, t)}{N}. \tag{2}$$

The relative probability of the ME front is defined as the ratio between the number of ME fronts and that of mesoscale eddies,

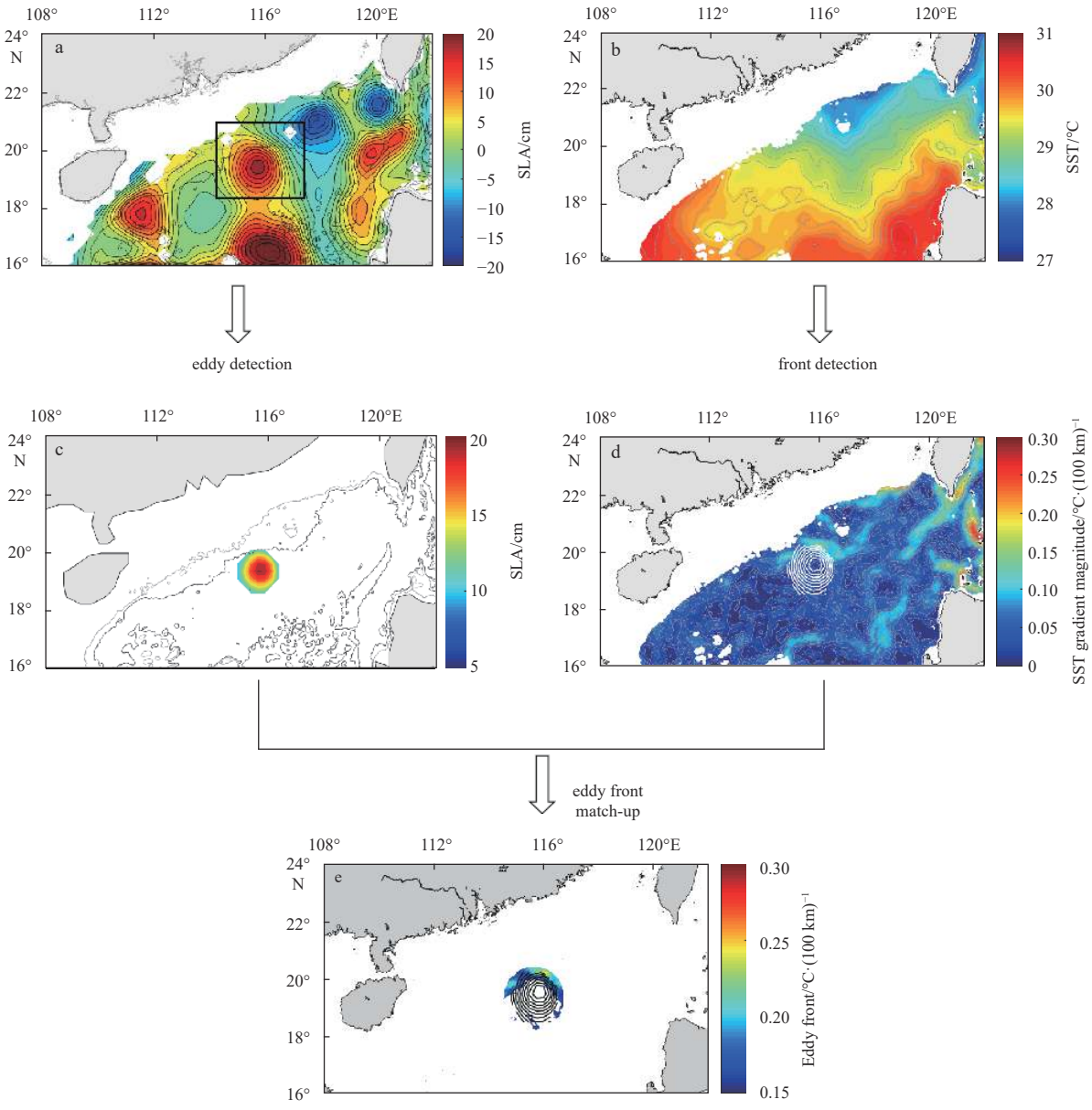

Fig. 1. Case study of ME front detection on May 30, 2015. Sea level anomaly (a), sea surface temperature (b), SLA of anticyclone eddy (colors) (c), anticyclone (white line) and SST gradient magnitude (colors) (d), and mesoscale eddy (black lines) and mesoscale eddy front (colors) (e). The gray lines in c are isobaths.

$$P_{\mathrm{r}}(x,y)=\frac{\sum_{t=1}^{N}\mathrm{MEF}(x,y,t)}{\sum_{t=1}^{N}\mathrm{ME}(x,y,t)}. \tag{3}$$

Although the spatial resolution of satellite SSTs (~5 km) is too coarse to investigate the fine structures of the ME front, it can indicate the presence or absence of the ME front. Hosoda et al. (2012) have attempted to examine multiple scales of oceanic fronts using microwave SSTs with spatial resolutions of 25 km. It is feasible to detect the presence of an ME front using OSTIA SST products.

3 Case study of ME fronts

We examined a warm eddy from April 19 to June 15, 2015. The SST gradient magnitude map shows that the ME front appeared at the interface between a warm eddy and a cold eddy (Fig. 1e). The three-dimensional structure and track of this eddy were previously reported in Qiu et al. (2019b). The SLA and SST anomaly maps of the eddy on May 30 are shown in Fig. 2a. The SST gradient magnitude along the glider track exceeded 0.2°C/km, reaching the SST front threshold (Fig. 2b). The length of this SST front is approximately 200 km.

We calculated vertical velocities to identify the current across front. Since the geostrophic balance equation may be unsuitable for the ME front, we obtained the vertical velocity w using the density conservation equation (Yu et al., 2019) as follows:

$$\frac{\partial\rho}{\partial t}+u\frac{\partial\rho}{\partial x}+v\frac{\partial\rho}{\partial y}+w\frac{\partial\rho}{\partial z}=0, \tag{4}$$

$$w = -\left(\frac{\partial \rho}{\partial t} + u\frac{\partial \rho}{\partial x} + v\frac{\partial \rho}{\partial y}\right) \Big/ \frac{\partial \rho}{\partial z}, \tag{5}$$

where ρ is the water density, as observed from Chinese underwater glider data; u and v are from the HYCOM data. We matched the HYCOM data with underwater glider data using a match-up window of 0.1° × 0.1°.

Vertical mean velocities at 200–800 m are shown in Fig. 2d. The alternation of upward (positive) and downward (negative) velocities within short distances (~10 km) indicates the appearance of complex current structures. Secondary circulation structures can develop vertically in the form of upwelling (downwelling) on the warmer (colder) side of the front (Capet et al., 2008). Our results show more complicated vertical circulation structures. The maximum vertical velocity was approximately 5×10^{-6} m/s (~4.3 m/d), which was equivalent to that in the northeastern Atlantic (Yu et al., 2019). These vertical velocities could lead to upward or downward heat transport.

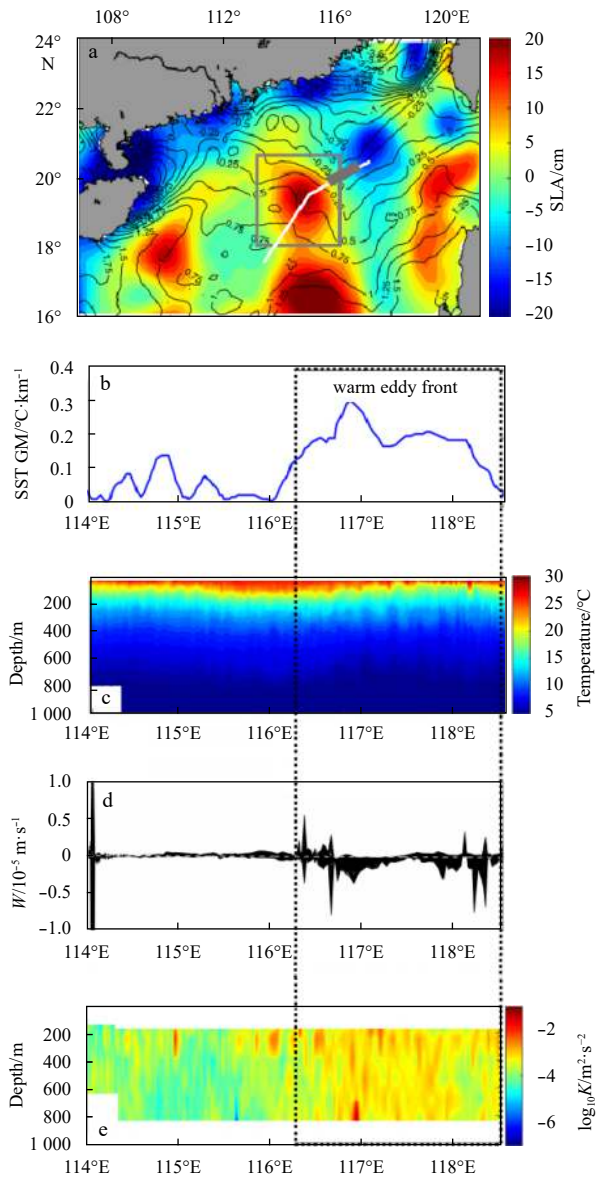

Fig. 2. Sea level anomalies (colors), sea surface temperature anomalies (black lines with interval of 0.25°C) on May 30, 2015 (a), SST gradient magnitude (b), contours of temperature (c), vertical velocity within surface 300 m (d), and vertical diffusion coefficient along the glider track (e). The white line indicates the Chinese underwater glider track. The black dashed box represents the front zone, where the SST GM>0.2°C/km. The vertical diffusion coefficient was calculated by the GHP method.

ME fronts may enhance the turbulent kinetic dissipation rate. Therefore, we calculated vertical mixing using Gregg-Henyey-Polzon (GHP) fine-scale parameterization (Henyey et al., 1986; Polzin et al., 2014; Gregg et al., 2003). This method has been successfully used in the SCS (Shang et al., 2017; Liang et al., 2017). The parameterization depends on fine-scale shear and strain variance, as follows:

$$K = K_0 \frac{\langle V_z^2 \rangle^2}{\mathrm{GM}\langle V_z^2 \rangle^2} h_1(R_w) j\left(\frac{f}{N}\right), \tag{6}$$

where K_0 is the reference dissipation rate (4.0×10^{-10} W/kg), GM $\langle V_z^2 \rangle$ is the shear variance from the GM model, and $\langle V_z^2 \rangle$ is the observed shear variance.

$$h_1(R_w) = \frac{3(R_w+1)}{2\sqrt{2}R_w\sqrt{R_w-1}}, \tag{7}$$

$$j\left(\frac{f}{N}\right) = \frac{f\mathrm{arcosh}(N/f)}{f_{30}\mathrm{arcosh}(N_0/f_{30})}, \tag{8}$$

where $f_{30}=f(30°\mathrm{N})$ and $N_0=3$ cph. $R_w=\dfrac{\langle V_z^2 \rangle}{\overline{N}^2 \langle \zeta_z^2 \rangle}$ is the shear/strain variance ratio, which is approximately 7. The strain variance $\langle \zeta_z^2 \rangle$ is estimated from buoyancy frequency, $\langle \zeta_z^2 \rangle = \left\langle (N^2-\overline{N}^2)^2/\overline{N}^4 \right\rangle$. Equation (6) can be determined by the strain variance and R_w,

$$K = K_0 \frac{\langle \zeta_z^2 \rangle^2}{\mathrm{GM}\langle \zeta_z^2 \rangle^2} h_2(R_w) j\left(\frac{f}{N}\right), \tag{9}$$

$$h_2(R_w) = \frac{R_w(R_w+1)}{6\sqrt{2}\sqrt{R_w-1}}. \tag{10}$$

The turbulent dissipation rate, K, is shown in Fig. 2e. Note that K value was very high at the front zone. Enhanced turbulence has been reported for the Kuroshio Current and California fronts (D'Asaro et al., 2011; Johnston et al., 2011). In this study, K is around 10^{-4} W/kg, larger than that at the ME periphery value observed by Yang et al. (2017). This difference may be due to limitations in the GHP method, which should be used in internal wave-breaking zones (Polzin et al., 2014). Liu et al. (2017) found that the GHP method was not appropriate for the low-latitude northwestern Pacific zone but could show enhanced vertical mixing at the ME boundary. This means that the spatial variation in K is reliable. Yu et al. (2019) suggested that frontogenesis, not frontolysis, can contribute to high turbulence. We also found that some fronts were not associated with increased turbulence (Qiu et al., 2017a). Thus, the enhanced turbulence at the ME front may be induced by frontogenesis.

4 Statistical analysis of ME fronts

4.1 *Spatial variations in the ME front*

Using the ME front detection method described in Section

2.2, we obtained ME front probabilities (Fig. 3). Figures 3a and b show the relative probabilities of the anticyclonic front (AEF) and cyclonic front (CEF). Both AEFs and CEFs had high frequencies (~20%) in the western Luzon Strait and off eastern Hainan Island; thus, approximately five MEs are overlapped with one ME front. The absolute probabilities of AEFs and CEFs were less than 6% in most regions (Figs 3c and d). The highest frequencies of both AEFs and CEFs were observed in the Luzon Strait, which had the highest EKE in the SCS (Zhuang et al., 2010). AEFs were more frequent than CEFs, especially in the western boundary of the SCS. More AEFs were found in the northern part (>20°N) than in the southern part of the NSCS. The total number of ME fronts was high (>150 times) along the western boundary (Figs 3e and f), where MEs intruded the continental slope, and easily produced submesoscale structures and a high turbulent kinetic dissipation rate (Zhang et al., 2016; Yang et al., 2019; Su et al., 2020).

Mesoscale eddies are asymmetric, so the ME front should have directions around the eddy center. Taking (x_0, y_0) as the eddy center, the radial frontal direction can be given by the following equation:

$$\begin{cases} A(x_0, y_0) = \arctan\dfrac{(y-y_0)}{(x-x_0)}, & x > x_0, y > y_0; \\ A(x_0, y_0) = 2\pi + \arctan\dfrac{(x-x_0)}{(y-y_0)}, & x > x_0, y < y_0; \\ A(x_0, y_0) = \pi + \arctan\dfrac{(y-y_0)}{(x-x_0)}, & x < x_0; \end{cases} \quad (11)$$

where (x_0, y_0) is the center position of the mesoscale eddies and (x, y) is the position of the ME front.

Then, we calculated the probability of AEF and CEF angles at intervals of π/4. The probability maps for AEF and CEF angles are shown in Fig. 4. More than 60% of fronts occurred in the northeastern and southwestern parts of anticyclonic MEs, and less than 40% of fronts occurred in the other two directions. CEFs were almost equally distributed around the cyclonic eddy center, with ~12% in each direction. These results indicate that anticyclones are more asymmetrical than cyclones.

4.2 *Temporal variations in the ME front*

Seasonal variations in AEFs and CEFs numbers are shown in

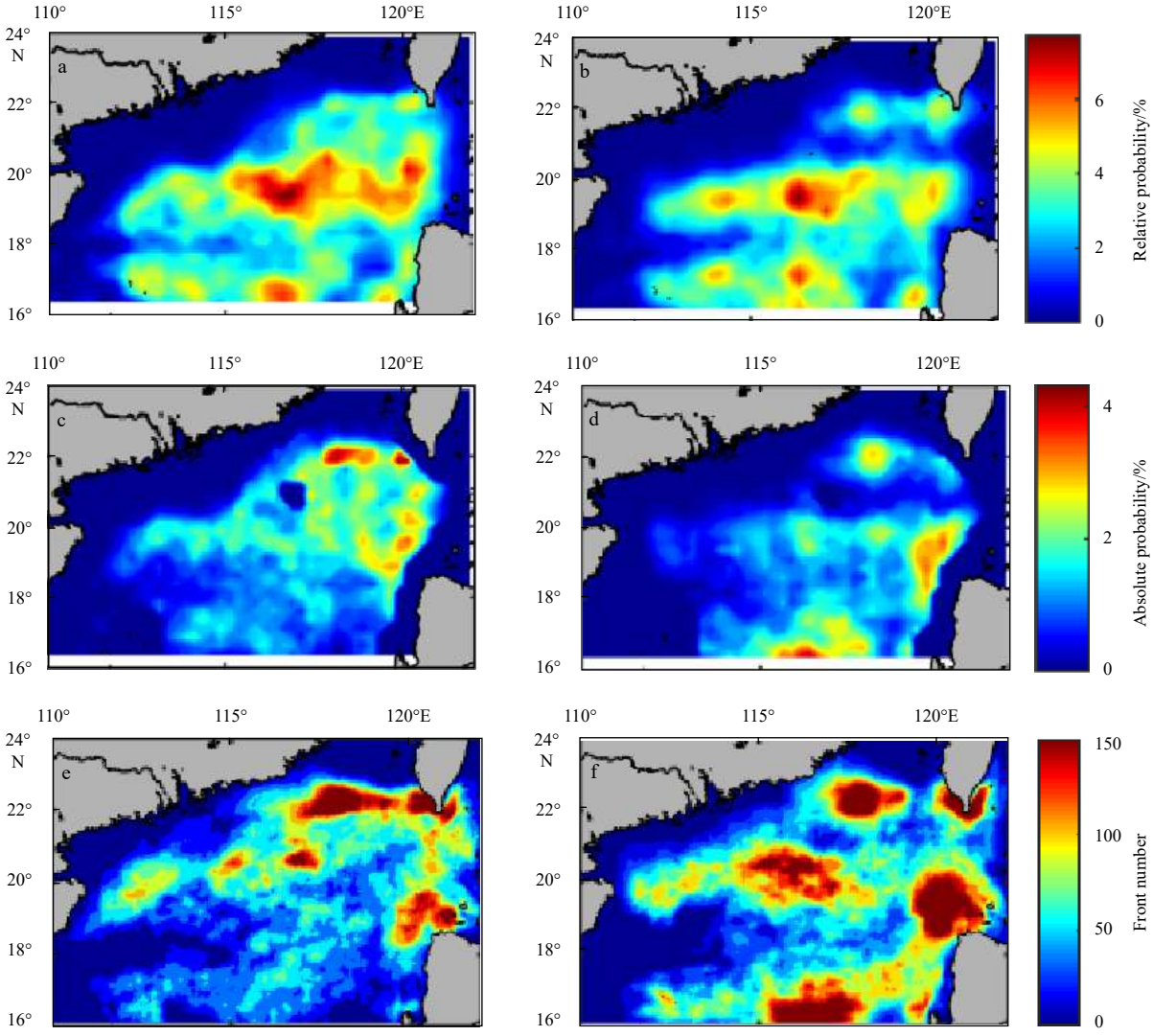

Fig. 3. Relative probability of ME fronts for anticyclones (a), relative probability of ME fronts for cyclones (b), absolute probability of ME fronts for anticyclones (c), absolute probability of ME fronts for cyclones (d), anticyclonic front number (e), and cyclonic front number (f).

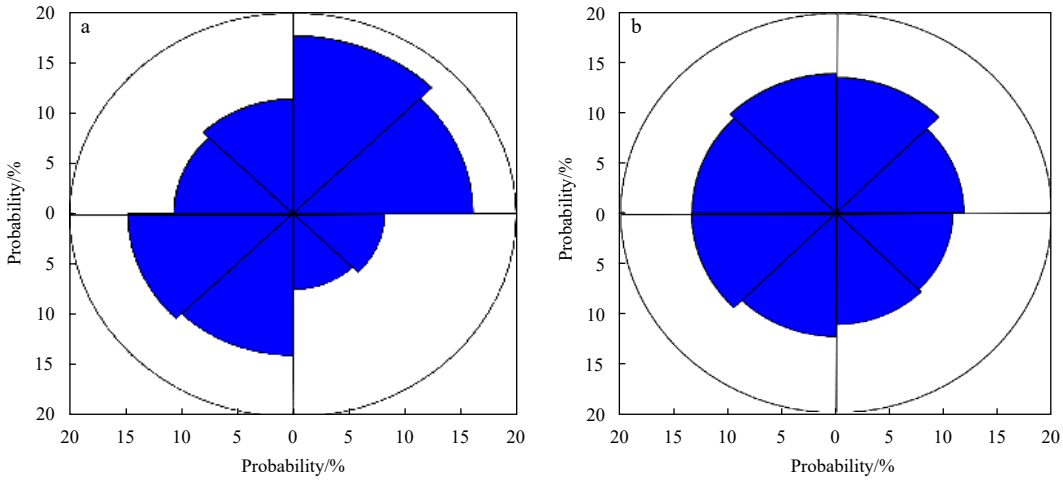

Fig. 4. The probability of ME front directions for anticyclones (a) and cyclones (b) every π/4.

Fig. 5. The number of CEFs has a significant seasonal variation, with a maximum value in February (6×10^5 pixels) and minimum value in September (~0). The number of CEFs exhibited the same seasonal trend as that of generated cyclones, which was suggested to be induced by wind stress curl offshore Luzon Strait and vorticity advection from the Kuroshio Current (Wang et al., 2008; Nan et al., 2011). Seasonal variation in AEFs was not apparent, although AEFs were slightly more frequent from November to March. This is different from the variation of anticyclones, which have significant seasonal variation with larger/smaller numbers in summer/winter due to monsoon-driven positive/negative wind stress curl (Chen et al., 2009). The smaller number of AEFs might result from the decrease in frontal numbers in summer, when solar radiation is almost uniform in the NSCS.

To investigate the dynamic process of ME fronts, we calculated the surface eddy kinetic energy (EKE) using $\mathrm{EKE}=(u'^2+v'^2)/2$, where $u'=-\frac{g}{f}\frac{\partial(\mathrm{SLA})}{\partial y}$, and $v'=-\frac{g}{f}\frac{\partial(\mathrm{SLA})}{\partial x}$ are geostrophic velocity anomalies. g is the acceleration due to gravity, and f is the Coriolis parameter. The seasonal variations in the mean EKEs are shown in Fig. 5b. There is no remarkable seasonal variation in EKE for AEFs and CEFs. Although the number of AEFs is small, the mean EKE in AEFs was quite large in summer. It is clear that the EKE in AEFs was larger than that in CEFs in all the months. The baroclinic front in an AEF is more unstable than that in an CEF (Brannigan, 2016), which may induce EKE to be stronger in AEFs than in CEFs.

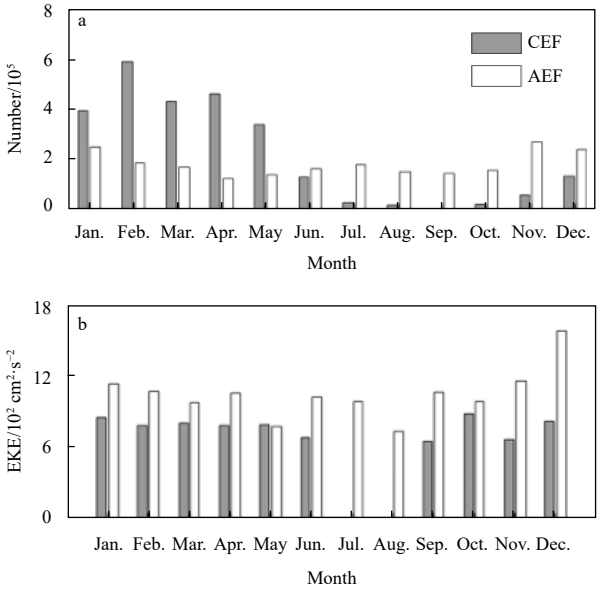

Fig. 5. Monthly variations in the number of ME fronts (a) and EKE at ME fronts (b). CEFs and AEFs are represented in gray and white colors, respectively.

Interannual variations in the numbers of AEFs and CEFs are shown in Fig. 6. The frontal number increased from 2007 to 2010 and then decreased from 2010 to 2018. We compared the numbers of ME fronts with the Niño 3.4 index (Niño 3.4 index; SST anomaly at 5°S to 5°N, 170°W to 120°W). The number of AEF/CEF and ENSO index were not significantly correlated, with coefficient values of –0.3/–0.23. This result is consistent with that revealed by Tuo et al. (2019), who found that the El Niño index and the number of MEs were not significantly correlated after 2004.

The total EKE at the ME front and within the eddy are shown in Figs 6c and d. The EKE magnitudes for CEF/AEF have the same trends as those for cyclones/anticyclones. That is when the frontal EKE was strong, the eddy EKE was also strong; thus, the frontal EKE magnitude contributed to the strength of the ME. The total EKE magnitudes were 4 500 and 8 000 cm^2/s^2 for CEFs and AEFs and 2 000 and 2 100 cm^2/s^2 for cyclones and anticyclones, respectively. The ME frontal mean EKE magnitudes were nearly 3-fold those of the MEs.

5 Possible mechanisms of ME fronts

The SST fronts at the ME edge (ME fronts) may include many processes, including horizontal discrepancies in air-sea heat exchange, wind-induced Ekman current advection, coastal current advection, mesoscale eddy straining, geostrophic disturbance and ageostrophic movement (Hoskins, 1974; Stone and Nemet, 1996). The SST tendency can be calculated from the mixed layer slab model (De Ruijter, 1983). The SST tendency in the radial direction is as follows:

$$\frac{\partial \mathrm{SST}}{\partial t}=-\frac{Q}{\rho c_p h}+V_r\frac{\partial \mathrm{SST}}{\partial r}+w\frac{\partial T}{\partial z}+R. \tag{12}$$

The four terms on the right-hand side are air-sea heat fluxes, ad-

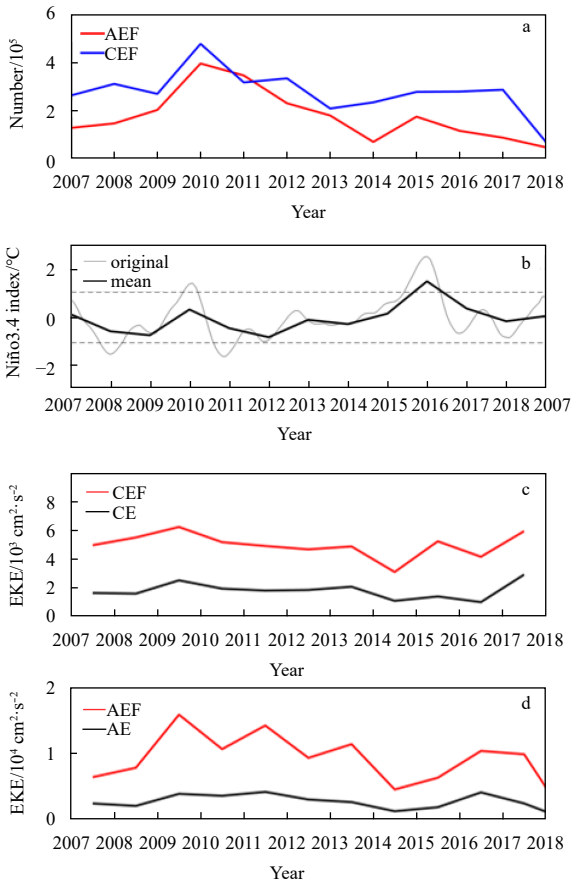

Fig. 6. Time series of numbers of anticyclone fronts (red) and cyclone fronts (blue) (a), Niño3.4 index (b), EKE at cyclone front (c), and EKE at anticyclone front (d). The black and gray lines in b are the annual mean and monthly ENSO index, respectively. The red lines in c and d are the mean EKE magnitudes at the eddy front zone, and black lines are the mean EKE magnitudes within the eddy.

vection, entrainment and diffusion terms. Q is the air-sea net heat flux, and h is the mixed layer depth. V_r and w are the radial and vertical velocities, respectively. T is the temperature at the bottom of the mixed layer. ρ and c_p are the sea water density and specific heat capacity. The tendency of the SST gradient magnitude at the edge of the mesoscale eddy can be obtained by taking the r derivation for Eq. (12),

$$\frac{\partial}{\partial t}\left(\frac{\partial \mathrm{SST}}{\partial r}\right) = -\frac{1}{\rho c_p}\frac{\partial}{\partial r}\left(\frac{Q}{h}\right) + \frac{\partial V_r}{\partial r}\frac{\partial \mathrm{SST}}{\partial r} + V_r\frac{\partial}{\partial r}\left(\frac{\partial \mathrm{SST}}{\partial r}\right) + \frac{\partial}{\partial r}\left(w\frac{\partial T}{\partial z}\right) + \frac{\partial}{\partial r}(R). \quad (13)$$

The air-sea heat flux term in Eq. (13) is difficult to quantify due to the lack of high spatial resolution air-sea net flux products at the eddy edge. The radial velocity V_r is the ageostrophic current, which can improve the water exchange at the eddy edge (Su et al., 2018; Yang et al., 2019), and strengthen or weaken the SST front through advection processes.

Mesoscale eddies have been proven to modify SST fronts in previous studies. Eddy straining is a frontogenesis mechanisms and has submesoscale characteristics (Capet et al., 2008; Brannigan, 2016). Eddy straining or deformation and asymmetry are suggested to be influenced by background large-scale currents, i.e., wind-driven currents and Kuroshio Current (Qiu et al., 2019b). In the NSCS, submesoscale structures are also active (Yang et al., 2017; Qiu et al., 2019a; Zheng et al., 2008). Dong and Zhong (2018) examined the spatiotemporal features of submesoscale processes and found that these processes are strong in winter and weak in summer. Their generation mechanisms have been revealed by Zhang et al. (2020).

SST fronts in the NSCS have both mesoscale/large-scale (Re<1) and submesoscale (Re~O(1)) structures (Wang et al., 2001; Jing et al., 2015; Zhong et al., 2017). In our case study (Fig. 2), the Rossby number of the SST front is Re<1 with a spatial range of 200 km and a mean horizontal velocity of 0.5 m/s. Therefore, this front is a meso/large scale front. However, at the warm and cold eddy edge, two narrow maximum vertical velocity zones with widths of ~10 km occurred (Fig. 2d), which are characteristic of submesoscale structures (Re~O(1)). This indicates that a large-scale SST front also includes submesoscale structures at the mesoscale eddy edge. To quantify the contributions of mesoscale eddies on the SST fronts, high spatial resolution observational data sets, including air-sea heat fluxes and oceanic physical parameters (temperature, salinity and velocity), are needed in the future studies.

6 Summary

Using satellite data, we developed an automatic integrated method to detect ME SST fronts in the NSCS and examined their spatiotemporal variations. ME fronts occupied 20% of the MEs; the northeast and southwest parts of anticyclones were more prone to generating fronts. Mean EKE values at the ME fronts were three times those of the MEs. CEFs were more common from winter to spring, and AEFs were common in all months. The EKE in an AEF was larger than that in an CEF, which might be due to the different levels of AEFs and CEFs.

The results of the current study can be used as a benchmark for future *in situ* ME front observations. We only detected SST fronts overlapping at the edge of the ME, which may be one part of a large-scale SST front, and the mesoscale eddy only modulates one part of the large SST front. We need to quantify the mesoscale eddy contributions on ME fronts by using high spatiotemporal resolution *in situ* data in the future.

Acknowledgements

Chinese underwater glider data were provided by State Key Laboratory of Robotics, Shenyang Institute of Automation, Chinese Academy of Science. We thank the AVISO (http://www.aviso.oceanobs.com/en/data/products/sea-surface-height-products/global/index.html) for sea level anomaly data, HYCOM for current velocity data, and OSTIA (http://ghrsst-pp.metoffice.com/pages/latest_analysis/ostia.html) for SST data.

References

Brannigan L. 2016. Intense submesoscale upwelling in anticyclonic eddies. Geophysical Research Letters, 43(7): 3360–3369, doi: 10.1002/2016GL067926

Capet X, McWilliams J C, Molemaker M J, et al. 2008. Mesoscale to submesoscale transition in the California current system. Part I: Flow structure, eddy flux, and observational tests. Journal of Physical Oceanography, 38(1): 29–43, doi: 10.1175/2007JPO3671.1

Chaigneau A, Gizolme A, Grados C. 2008. Mesoscale eddies off Peru in altimeter records: Identification algorithms and eddy spatio-temporal patterns. Progress in Oceanography, 79(2–4): 106–119

Chen Gengxin, Hou Yijun, Chu Xiaoqing, et al. 2009. The variability of eddy kinetic energy in the South China Sea deduced from satel-

lite altimeter data. Chinese Journal of Oceanology and Limnology, 27(4): 943–954, doi: 10.1007/s00343-009-9297-6
Cheng Xuhua, Qi Yiquan. 2010. Variations of eddy kinetic energy in the South China Sea. Journal of Oceanography, 66(1): 85–94, doi: 10.1007/s10872-010-0007-y
D'Asaro E, Lee C, Rainville L, et al. 2011. Enhanced turbulence and energy dissipation at ocean fronts. Science, 332(6027): 318–322, doi: 10.1126/science.1201515
De Ruijter W P M. 1983. Effects of velocity shear in advective mixed-layer models. Journal of Physical Oceanography, 13(9): 1589–1599, doi: 10.1175/1520-0485(1983)013<1589:EOVSIA>2.0.CO;2
Dong Jihai, Zhong Yisen. 2018. The spatiotemporal features of submesoscale processes in the northeastern South China Sea. Acta Oceanologica Sinica, 37(11): 8–18, doi: 10.1007/s13131-018-1277-2
Donlon C J, Martin M, Stark J, et al. 2011. The operational sea surface temperature and sea ice analysis (OSTIA) system. Remote Sensing of the Environment, 116: 140–158
Feng Baoxin, Liu Hailong, Lin Pengfei. 2020. Effects of Kuroshio intrusion optimization on the simulation of mesoscale eddies in the northern South China Sea. Acta Oceanologica Sinica, 39(3): 12–24, doi: 10.1007/s13131-020-1565-5
Gregg M C, Sanford T B, Winkel D P. 2003. Reduced mixing from the breaking of internal waves in equatorial waters. Nature, 422(6931): 513–515, doi: 10.1038/nature01507
Henyey F S, Wright J, Flatté S M. 1986. Energy and action flow through the internal wave field: An eikonal approach. Journal of Geophysical Research: Oceans, 91(C7): 8487–8495, doi: 10.1029/JC091iC07p08487
Hoskins B J. 1974. The role of potential vorticity in symmetric stability and instability. Quarterly Journal of Royal Meteorology Society, 100(425): 480–482, doi: 10.1002/qj.49710042520
Hosoda K, Kawamura H, Lan K W, et al. 2012. Temporal scale of sea surface temperature fronts revealed by microwave observations. IEEE Geoscience and Remote Sensing Letters, 9(1): 3–7, doi: 10.1109/LGRS.2011.2158512
Hu Jianyu, Zheng Quanan, Sun Zhenyu, et al. 2012. Penetration of nonlinear Rossby eddies into South China Sea evidenced by cruise data. Journal of Geophysical Research: Oceans, 117(C3): C03010
Huang Xiaodong, Zhang Zhiwei, Zhang Xiaojiang, et al. 2017. Impacts of a mesoscale eddy pair on internal solitary waves in the northern South China Sea revealed by mooring array observations. Journal of Physical Oceanography, 47(7): 1539–1554, doi: 10.1175/JPO-D-16-0111.1
Jing Zhiyou, Qi Yiquan, Du Yan, et al. 2015. Summer upwelling and thermal fronts in the northwestern South China Sea: Observational analysis of two mesoscale mapping surveys. Journal of Geophysical Research: Oceans, 120(3): 1993–2006, doi: 10.1002/2014JC010601
Johnston T, Rudnick D, Pallàs-Sanz E. 2011. Elevated mixing at a front. Journal of Geophysical Research: Oceans, 116(C11): C11033, doi: 10.1029/2011JC007192
Lévy M, Klein P, Tréguier AM. 2001. Impact of sub-mesoscale physics on production and subduction of phytoplankton in an oligotrophic regime. Journal of Marine Research, 59(4): 535–565, doi: 10.1357/002224001762842181
Liang Changrong, Chen Guiying, Shang Xiaodong. 2017. Observations of the turbulent kinetic energy dissipation rate in the upper central South China Sea. Ocean Dynamics, 67(5): 597–609, doi: 10.1007/s10236-017-1051-6
Liu Zhiyu, Lian Qiang, Zhang Fangtao, et al. 2017. Weak thermocline mixing in the North Pacific low-latitude western boundary current system. Geophysical Research Letters, 44(20): 10530–10539, doi: 10.1002/2017GL075210
McWilliams J C. 2016. Submesoscale currents in the ocean. Proceedings of the Royal Society A—Mathematical, Physical and Engineering Sciences, 472(2189): 20160117, doi: 10.1098/rspa.2016.0117
Nan Feng, Xue Huijie, Xiu Peng, et al. 2011. Oceanic eddy formation and propagation southwest of Taiwan. Journal of Geophysical Research: Atmospheres, 116(C12): C12045, doi: 10.1029/2011JC007386
Polzin K L, Garabato A C N, Huussen T N, et al. 2014. Finescale parameterizations of turbulent dissipation. Journal of Geophysical Research: Oceans, 119(2): 1383–1419, doi: 10.1002/2013JC008979
Qiu Chunhua, Cui Yongsheng, Hu Shiqi, et al. 2017a. Seasonal variation of Guangdong coastal thermal front based on merged satellite data. Journal of Tropical Oceanography (in Chinese), 36(5): 16–23
Qiu Chunhua, Mao Huabin, Liu Hailong, et al. 2019a. Deformation of a warm eddy in the northern South China Sea. Journal of Geophysical Research: Oceans, 124(8): 5551–5564, doi: 10.1029/2019JC015288
Qiu Chunhua, Mao Huabin, Wang Yanhui, et al. 2019b. An irregularly shaped warm eddy observed by Chinese underwater gliders. Journal of Oceanography, 75(2): 139–148, doi: 10.1007/s10872-018-0490-0
Qiu Chunhua, Mao Huabin, Yu Jiancheng, et al. 2015. Sea surface cooling in the Northern South China Sea observed using Chinese sea-wing underwater glider measurements. Deep Sea Research Part I: Oceanographic Research Papers, 105: 111–118, doi: 10.1016/j.dsr.2015.08.009
Qiu Bo, Nakano T, Chen Shuiming, et al. 2017b. Submesoscale transition from geostrophic flows to internal waves in the northwestern Pacific upper ocean. Nature Communications, 8: 14055, doi: 10.1038/ncomms14055
Ruiz S, Claret M, Pascual A, et al. 2019. Effects of oceanic mesoscale and submesoscale frontal processes on the vertical transport of phytoplankton. Journal of Geophysical Research: Oceans, 124(8): 5999–6014, doi: 10.1029/2019JC015034
Sadarjoen I A, Post F H. 2000. Detection, quantification, and tracking of vortices using streamline geometry. Computers & Graphics, 24(3): 333–341
Shang Xiaodong, Liang Changrong, Chen Guiying. 2017. Spatial distribution of turbulent mixing in the upper ocean of the South China Sea. Ocean Science, 13(3): 503–519, doi: 10.5194/os-13-503-2017
Shu Yeqiang, Xiu Peng, Xue Huijie, et al. 2016. Glider-observed anticyclonic eddy in northern South China Sea. Aquatic Ecosystem Health & Management, 19(3): 233–241
Stone P H, Nemet B. 1996. Baroclinic adjustment: A comparison between theory, observations, and models. Journal of the Atmospheric Sciences, 53(12): 1663–1674, doi: 10.1175/1520-0469(1996)053<1663:BAACBT>2.0.CO;2
Su Danyi, Lin Pengfei, Mao Huabin, et al. 2020. Features of slope intrusion mesoscale eddies in the northern South China Sea. Journal of Geophysical Research: Oceans, 125(2): e2019JC015349
Su Zhan, Wang Jinbo, Klein P, et al. 2018. Ocean submesoscales as a key component of the global heat budget. Nature Communications, 9: 775, doi: 10.1038/s41467-018-02983-w
Sun Zhongbin, Zhang Zhiwei, Zhao Wei, et al. 2016. Interannual modulation of eddy kinetic energy in the northeastern South China Sea as revealed by an eddy-resolving OGCM. Journal Geophysical Research: Oceans, 121(5): 3190–3201, doi: 10.1002/2015JC011497
Torres H S, Klein P, Menemenlis D, et al. 2018. Partitioning ocean motions into balanced motions and internal gravity waves: A modeling study in anticipation of future space missions. Journal of Geophysical Research: Oceans, 123(11): 8084–8105, doi: 10.1029/2018JC014438
Tuo Pengfei, Yu Jinyi, Hu Jianyu. 2019. The changing influences of ENSO and the Pacific meridional mode on mesoscale eddies in the South China Sea. Journal of Climate, 32(3): 685–700, doi: 10.1175/JCLI-D-18-0187.1
Wang Guihua, Chen Dake, Su Jilan. 2008. Winter eddy genesis in the eastern South China Sea due to orographic wind jets. Journal of Physical Oceanography, 38(3): 726–732, doi: 10.1175/2007JPO3868.1
Wang Dongxiao, Liu Yun, Qi Yiquan, et al. 2001. Seasonal variability

of thermal fronts in the northern South China Sea from satellite data. Geophysical Research Letters, 28(20): 3963–3966, doi: 10.1029/2001GL013306

Wang Qiang, Zeng Lili, Li Jian, et al. 2018. Observed cross-shelf flow induced by mesoscale eddies in the northern South China Sea. Journal of Physical Oceanography, 48(7): 1609–1628, doi: 10.1175/JPO-D-17-0180.1

Xie Shangping. 2004. Satellite observations of cool ocean-atmosphere interaction. Bulletin of the American Meteorological Society, 85(2): 195–208, doi: 10.1175/BAMS-85-2-195

Yang Qingxuan, Nikurashin M, Sasaki H, et al. 2019. Dissipation of mesoscale eddies and its contribution to mixing in the northern South China Sea. Scientific Reports, 9: 556, doi: 10.1038/s41598-018-36610-x

Yang Qingxuan, Zhao Wei, Liang Xinfeng, et al. 2017. Elevated mixing in the periphery of mesoscale eddies in the South China Sea. Journal of Physical Oceanography, 47(4): 895–907, doi: 10.1175/JPO-D-16-0256.1

Yu Xiaolong, Garabato A C N, Martin A P, et al. 2019. An annual cycle of submesoscale vertical flow and restratification in the upper ocean. Journal of Physical Oceanography, 49(6): 1439–1461, doi: 10.1175/JPO-D-18-0253.1

Yuan Dongliang, Han Weiqing, Hu Dunxin. 2006. Surface Kuroshio path in the Luzon Strait area derived from satellite remote sensing data. Journal of Geophysical Research: Oceans, 111(C11): C11007, doi: 10.1029/2005JC003412

Zhang Zhiwei, Tian Jiwei, Qiu Bo, et al. 2016. Observed 3D structure, generation, and dissipation of oceanic mesoscale eddies in the South China Sea. Scientific Reports, 6: 24349, doi: 10.1038/srep24349

Zhang Zhiwei, Zhang Yuchen, Qiu Bo, et al. 2020. Spatiotemporal characteristics and generation mechanisms of submesoscale currents in the northeastern South China Sea revealed by numerical simulations. Journal of Geophysical Research: Oceans, 125(2): e2019JC015404

Zhang Zhiwei, Zhao Wei, Tian Jiwei, et al. 2013. A mesoscale eddy pair southwest of Taiwan and its influence on deep circulation. Journal of Geophysical Research: Atmospheres, 118(12): 6479–6494

Zheng Quanan, Lin Hui, Meng Junmin, et al. 2008. Sub-mesoscale ocean vortex trains in the Luzon Strait. Journal of Geophysical Research: Oceans, 113(C4): C04032

Zhong Yisen, Bracco A, Tian Jiwei, et al. 2017. Observed and simulated submesoscale vertical pump of an anticyclonic eddy in the South China Sea. Scientific Reports, 7: 44011, doi: 10.1038/srep44011

Zhuang Wei, Xie Shangping, Wang Dongxiao, et al. 2010. Intraseasonal variability in sea surface height over the South China Sea. Journal of Geophysical Research: Oceans, 115(C4): C04010